

Second Harmonic Generation Enabled by Longitudinal Electric Field Components in Photonic Wire Waveguides

Nicolas Poulvellarie,^{1,2,3} Utsav Dave,⁴ Koen Alexander,^{2,3} Charles Ciret,⁵ Maximilien Billet,^{1,2,3}

Carlos Mas Arabi,¹ Fabrice Raineri,^{6,7} Sylvain Combrié,⁸ Alfredo De Rossi,⁸

Gunther Roelkens,^{2,3} Simon-Pierre Gorza,¹ Bart Kuyken,^{2,3} and François Leo^{1,*}

¹ OPERA-Photonique, Université libre de Bruxelles, Brussels, Belgium

² Photonics Research Group, Ghent University-IMEC, Ghent, Belgium

³ Center for Nano- and Biophotonics (NB-Photonics), Ghent University, Ghent, Belgium

⁴ Department of Electrical Engineering, Columbia University, New York, USA

⁵ Laboratoire de Photonique d'Angers EA 4464, Université d'Angers, Angers, France

⁶ Centre de Nanosciences et de Nanotechnologies (C2N), CNRS,

Univ. Paris Sud, Univ. Paris Saclay, F-91120 Palaiseau, France

⁷ Université de Paris, Centre de Nanosciences et de Nanotechnologies (C2N), F-91120 Palaiseau, France and

⁸ Thales Research and Technology, Palaiseau, France*

We investigate type I second harmonic generation in III-V semiconductor wire waveguides aligned with a crystallographic axis. Because of the single nonzero tensor element of III-V semiconductors, only nonlinear coupling through the mixing of transverse and longitudinal components of the optical fields is permitted. We experimentally study the impact of the propagation direction on the conversion efficiency and confirm the role played by the longitudinal components through the excitation of an antisymmetric second harmonic higher order mode.

Nanophotonic wire waveguides are well suited for efficient frequency conversion. The high index contrast allows to confine waves into sub-wavelength structures, greatly increasing the strength of light-matter interactions. Recent examples include ultra-efficient second harmonic (SH) generation [1, 2] and frequency comb formation [3, 4]. The bound modes propagating in high index contrast waveguides are very different from the well known transverse plane wave solutions of the Helmholtz equation [5]. In particular they possess a strong longitudinal component. In silicon wire waveguides for example, the amplitude of the longitudinal field can be almost as large as that of its transverse counterpart [6]. Having a large electric field pointing in the direction of propagation is of interest for applications such as linear accelerators [7], optical storage [8] or microscopy [9]. Yet, the strong longitudinal fields propagating in nanowaveguides are still to be harnessed for efficient nonlinear conversion.

Considering an instantaneous response, the field induced polarization components along three crystal axis (x, y, z) is most often approximated by the following expansion [10]:

$$P_i = \varepsilon_0 \left[\sum_j \chi_{ij}^{(1)} E_j + \sum_{jk} \chi_{ijk}^{(2)} E_j E_k + \dots \right] \quad (1)$$

where $i, j, k = x, y, z$. The linear response is diagonal in the crystal axis. In nanowaveguides, the longitudinal field induces coupling between modes through the $\chi_{zz}^{(1)}$ term [11]. Polarization rotators based on this principle have been implemented [12]. The impact of longitudinal components on the second order nonlinear polarization was studied in zinc selenide crystals, lithium niobate and gallium phosphide nanopillars [13–15] but, to the best of our knowledge, nonlinear coupling enabled by longitudi-

nal fields has never been demonstrated. Here, we detail how axially oscillating dipoles may be leveraged to excite an antisymmetric SH wave in semiconductor wire waveguides, a process that is prohibited for purely transverse waves. Specifically, we theoretically and experimentally investigate type I second harmonic generation in indium gallium phosphide (InGaP) wire waveguides.

III-V semiconductors are arranged in a zinc blende configuration ($\bar{4}3m$ point group) that leaves only the nondiagonal $\chi_{xyz}^{(2)}$ element nonzero. It was measured to be as high as 220 pm/V in InGaP [16]. The corresponding effective nonlinearity can be theoretically evaluated by perturbation analysis of the linear bound modes. The calculation is detailed in [22], we only report the main steps. A similar scheme has been applied to difference frequency generation [17] as well as third order nonlinearities [11, 18–21]. The coordinates in the waveguide frame are $(x'y'z')$. We only consider waveguides fabricated in the xz (010) plane of the crystal. The fields are a superposition of two forward propagating modes:

$$\vec{E} = \Re \{ a(z') \vec{e}_a e^{i(\beta_a z' - \omega_0 t)} + b(z') \vec{e}_b e^{i(\beta_b z' - 2\omega_0 t)} \}, \quad (2)$$

$$\vec{H} = \Re \{ a(z') \vec{h}_a e^{i(\beta_a z' - \omega_0 t)} + b(z') \vec{h}_b e^{i(\beta_b z' - 2\omega_0 t)} \}. \quad (3)$$

where ω_0 is the carrier frequency of the pump mode, a, b are the amplitudes of the modes [expressed in \sqrt{W}] and β_a, β_b are their propagation constants. The orthonormal spatial distributions of the electric and magnetic fields satisfy:

$$\frac{1}{2} \int \{ \vec{e}_i^* \times \vec{h}_j \} \cdot \hat{z}' dA = \delta_{ij}. \quad (4)$$

where $\vec{e}(\vec{r}'_{\perp}, \omega_j)$ and $\vec{h}(\vec{r}'_{\perp}, \omega_j)$ are the vectorial electric and magnetic mode profile. Both the profiles and propagation constants can be computed with commercial mode

solvers. The longitudinal components have a fixed phase difference of $\pi/2$ with their transverse counterparts. We choose to work with real transverse components such that the longitudinal components are purely imaginary. Accordingly, we introduce the imaginary part of the longitudinal component $e^{z'_i} = -ie^{z'}$ which allows to use purely real spatial distributions in what follows. Applying the theoretical framework based on the reciprocity theorem (see e.g. [11] and references therein), we find that the mode amplitudes obey the following propagation equations:

$$\frac{da(z')}{dz'} = -\alpha_a a(z') + i\kappa^*(\theta)b(z')a^*(z')e^{-i\Delta\beta z'}, \quad (5)$$

$$\frac{db(z')}{dz'} = -\alpha_b b(z') + i\kappa(\theta)a^2(z')e^{i\Delta\beta z'}. \quad (6)$$

where $\Delta\beta = 2\beta_a - \beta_b$ and θ is the angle between the propagation direction z' and the [100] axis (See Fig. 1). In the crystal axis, the effective nonlinearity simply reads:

$$\kappa = \frac{\omega_0 \varepsilon_0}{2} \int \chi_{xyz}^{(2)} (e_b^{*x} e_a^y e_a^z + e_b^{*y} e_a^x e_a^z + e_b^{*z} e_a^x e_a^y) dA. \quad (7)$$

The nonlinearity changes sign every 90° , as dictated by the 4 symmetry of the material such that we can limit the discussion to the first quadrant. The conversion efficiency is either maximum at 0° or 45° depending on the spatial distributions of the modes [22]. The effective nonlinearity characterizing the coupling between modes propagating along the [100] crystal axis reads:

$$\kappa(0^\circ) = \frac{i\omega_0 \varepsilon_0}{2} \int \chi_{xyz}^{(2)} (e_b^{x'} e_a^{y'} e_a^{z'_i} + e_b^{y'} e_a^{x'} e_a^{z'_i} - e_b^{z'_i} e_a^{x'} e_a^{y'}) dA. \quad (8)$$

where we introduced the imaginary part of the longitudinal components. We readily see that the longitudinal fields play a critical role in waveguides aligned with a crystal axis as there can be no conversion between purely transverse waves. A 45° rotation around the [010] axis yields a very different effective nonlinearity :

$$\kappa(45^\circ) = \frac{\omega_0 \varepsilon_0}{2} \int \chi_{xyz}^{(2)} \left[e_a^{y'} (e_b^{x'} e_a^{x'} - e_b^{z'_i} e_a^{z'_i}) + \frac{e_b^{y'}}{2} (e_a^{x'^2} + e_a^{z'_i^2}) \right] dA. \quad (9)$$

Here, transverse components can efficiently mix and the longitudinal components contribution is usually small. When a mirror symmetry is present [see Fig. 1 (b)], spatial distributions $e_{a,b}$ are either symmetric or antisymmetric in the corresponding direction [see Fig. 1 (b)]. Importantly, the different profiles of a same mode display different symmetries. A symmetric (resp. antisymmetric) e^x implies an antisymmetric (resp. symmetric) e^y and e^z [5]. This has important consequences for the overlap integrals in eq (8) and (9). Second harmonic modes with a certain symmetry can only be efficiently

excited in a specific direction. The modes with a symmetric longitudinal profiles at 45° and the modes with an antisymmetric longitudinal profile at 0° . Note that the symmetry of the pump mode has no impact because two pump photons are involved in the process. There are hence two experimental signatures of second harmonic generation induced by longitudinal components in InGaP wire waveguides: (i) the propagation direction that maximizes the conversion efficiency should be aligned with a crystallographic axis and (ii) the vertical component of the second harmonic mode e_b^y should be antisymmetric.

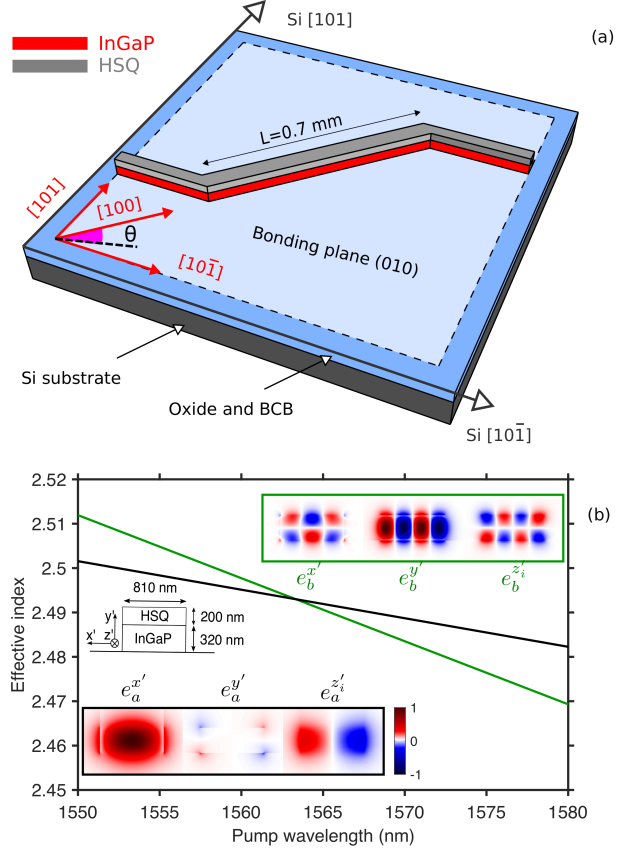


FIG. 1: (a) Schematic of a 320 nm high, 810 nm wide III-V-on-insulator waveguide with both 0° and 45° sections. (b) Simulated effective indices of the corresponding pump TE_{00} and SH TM_{30} modes showing phase matching around 1560 nm. The waveguide cross section as well as the spatial profile of the electric field components are shown as inset.

We fabricate waveguides in an epitaxially grown Indium Gallium Phosphide thin layer bonded on a silicon wafer [23]. We start with a waveguide made of both 0° and 45° sections [see Fig. 1 (a)]. The cleave directions of both silicon and InGaP are along the [101] and $[10\bar{1}]$ axis, such that the middle section ($L = 700 \mu\text{m}$) is aligned with the crystallographic axis. The waveguide is 320 nm high and 810 nm wide. Mode solver simulations predict phase matching between a quasi- TE_{00} pump mode and a quasi- TM_{30} second harmonic mode. The dependence

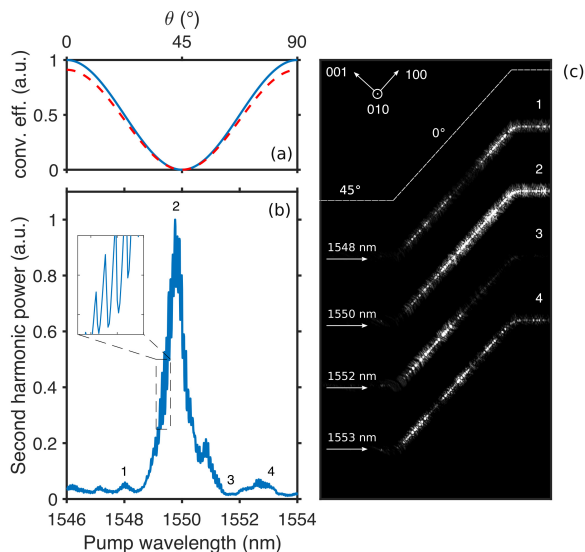


FIG. 2: (a) Blue line: Theoretical conversion efficiency $[\kappa(\theta)]^2$ corresponding to the coupling shown in Fig. 1. Red dotted line: Same when only the $e_b^y e_a^x e_a^{z_i}$ term of equation 7 is taken into account. (b) Detected second harmonic versus pump wavelength. A close up of the Fabry Perot fringes (FSR = 7.5 pm) is shown in the inset. (c) Diffusion patterns (top view) recorded on a silicon camera for different pump wavelengths. They are shifted vertically from one another. The solid line indicates the position of the 0° and 45° sections. The intensity has been normalized in each case so as to show the patterns more clearly.

of the corresponding effective nonlinearity with the propagation direction is shown in Fig 2(a). Also shown is the amplitude of the middle term ($e_b^y e_a^x e_a^{z_i}$) of eq. (7) to highlight that the interaction is dominated by the mixing of these three components. The maximum conversion corresponds to $\kappa(0^\circ) = 260i(\sqrt{\text{Wm}})^{-1}$. No conversion is expected for $\theta = 45^\circ$.

We launch horizontally polarized light from a tunable C band laser in the waveguide through a lensed fiber. The output waves are collected by use of an objective with a large numerical aperture (NA=0.9). The experimental phase matching function is shown in Fig 2(b). We find maximum conversion close to 1550 nm with a conversion bandwidth of 0.6 nm. The fast oscillations (see inset) are due to the Fabry Perot cavity induced by Fresnel reflection on both facets of the waveguide. The measured 7.5 pm free spectral range matches very well with the theoretical 7.8 pm corresponding to a 4.4 mm long waveguide with a group index $n_g = 3.5$. We also image the SH diffusion pattern from the top of the waveguide with a silicon camera for pump wavelengths corresponding to local extremas of the phase matching function [see Fig 2(c)]. Around the maximum conversion, the SH wave appears shortly after the first turn and increases until the 0° section ends. This confirms our prediction that the nonlinear conversion occurs only in the waveguide aligned

with the crystallographic axis. Around 1548 nm we find a pattern of SH generation and parametric down conversion akin to what is predicted by integrating eq. (6) for $\Delta\beta = \pm 3\pi/L$ [10]. When pumping at 1553 nm however, the measurement is reminiscent of the dynamics expected for $\Delta\beta = \pm 5\pi/L$. This discrepancy is confirmed by pumping at 1552 nm where nonlinear conversion seems to take place only in the first half of the 0° section. The diffusion patterns and transfer function both indicate that the conversion dynamics is different on both sides of the maximum conversion point, a behaviour we could not replicate by integrating (5) and (6). Asymmetric phase matching functions have been found in other SHG experiments in nanowires [1, 2, 24, 25]. They are likely due to inhomogeneities of the waveguide cross section. A detailed study of inhomogeneities on SH pattern is beyond the scope of the present report. Importantly, our experiments confirm the impact of the propagation direction on second harmonic generation in III-V nanowaveguides. The SH is most efficiently excited when the waveguide is aligned with a crystallographic axis, as theoretically predicted when the interaction is enabled by the longitudinal components of the modes.

In a second experiment, we aim to confirm whether these SH modes display the expected symmetry. To have access to the excited second harmonic mode without disturbance from bends and sections without conversion, we fabricate waveguides in an InGaP layer rotated with respect to the silicon wafer [see Fig. 3(a)]. In this case we used a positive-tone resist (ARP-6200) for the lithography and silicon nitride as a hard mask. We use waveguides with a 90° bend between sections of different width to be able to study different lengths while keeping the propagation direction fixed. Because of the sub-wavelength nature of the transverse profile, only certain higher order modes can be faithfully imaged. The large point spread function relative to the waveguide width prevents from reconstructing modes with more than one zero in the same direction. Hence we look to excite a mode with one zero in the x-direction and one or less zero in the y-direction, constrained by the fixed InGaP layer height of 320 nm. Simulations predict phase matching between a quasi-TM₀₀ pump mode and a quasi-TM₁₁ second harmonic mode in a 600 nm wide waveguide for a pump around 1590 nm. The corresponding theoretical effective nonlinearity is $\kappa(0^\circ) = -57i(\sqrt{\text{Wm}})^{-1}$. Note that none of the three terms of equation (8) are negligible in this case. All field components, including both longitudinal ones, play a crucial role in the nonlinear coupling.

We couple vertically polarized light from a tunable laser source into both waveguides through the 700 nm wide section by use of a lensed fiber. The output is collected with a high NA (0.9) objective. The maximum conversion is found at 1572 nm in the shorter waveguide (see Fig. 4). Through a Glan-Taylor prism, we analyze the polarization of the waves and find that both the

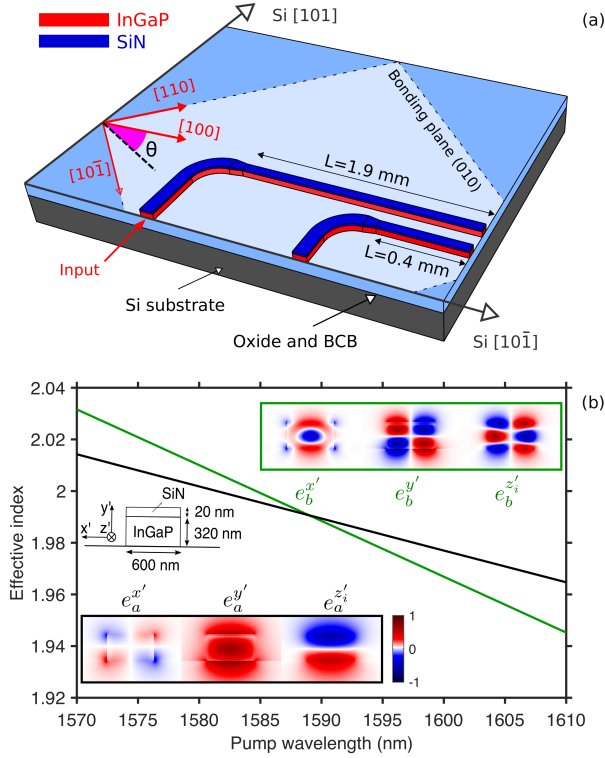


FIG. 3: (a) Schematic of two straight sections of different lengths of 320 nm high, 600 nm wide III-V-on insulator waveguides. Both are connected to a 700 nm wide section. (b) Simulated effective indices of the corresponding pump TM_{00} and SH TM_{11} modes showing phase matching around 1590 nm. The waveguide cross section as well as the spatial profile of the electric field components are shown as inset.

pump and SH are predominantly vertically polarized, as predicted by the full vectorial modeling. The output SH mode is imaged through a 4f telescope arrangement comprising our objective ($f = 1.8$ mm) and a plano-convex lens with a focal length of 750 mm. To calibrate our imaging system, we launch 775 nm light at the input of the waveguide to excite a fundamental mode around the second harmonic. We measure a profile very similar to the computed TE_{00} mode [Fig 4(c,e)] given the limited resolution of the imaging setup. We then image the output SH mode when pumping at 1572 nm and find excellent agreement between theoretical and experimental profiles [Fig 4(b,d)]. In the longer waveguide, we find a similar phase matching point around 1566 nm. The phase matching function is narrower, as expected, and the output mode profile confirms that we excite the same TM_{11} SH mode as in the short waveguide [Fig 4(g)]. As discussed above, different symmetries are expected for the different components. The vertically (resp. horizontally) polarized components should be antisymmetric (resp. symmetric) in the x' direction. To find out, we add the Glan-Taylor prism before the camera and record the image for both horizontal and vertical polarizations

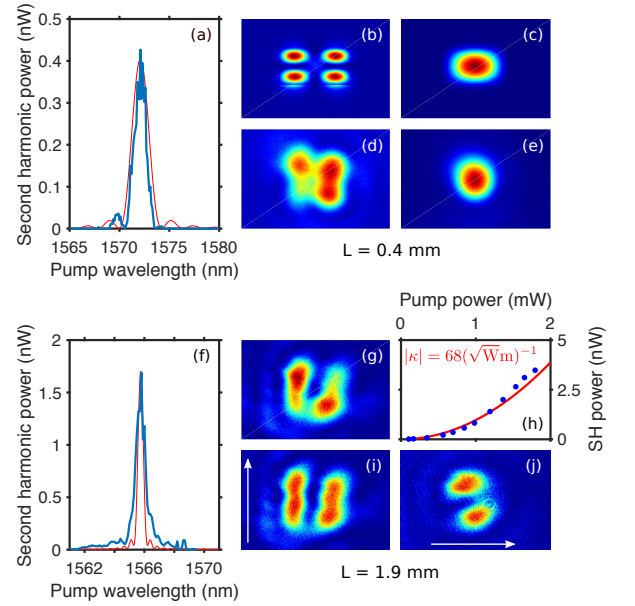


FIG. 4: Experimental results obtained with the waveguides shown in Fig. 3(a) Experimental (blue) and theoretical (red) SH harmonic power at the output of the short waveguide versus pump wavelength (input power = 2.5 mW). (b,c) Theoretical Poynting vector profile for the SH TM_{11} mode and TE_{00} mode. (d,e) Experimental profile of the SH TM_{11} mode and TE_{00} mode. The theoretical and experimental field of views are $1.27 \mu\text{m} \times 0.85 \mu\text{m}$ and $2.84 \mu\text{m} \times 1.89 \mu\text{m}$ respectively. (f) Experimental (blue) and theoretical (red) SH harmonic power at the output of the long waveguide versus pump wavelength (input power = 1.3 mW). (g) Experimental image of the SH TM_{11} mode at the output of the long waveguide. (h) Experimental (blue dots) and theoretical (red line) SH power as a function of the pump power when pumped at 1566 nm. (i,j) Experimental image of the SH mode after the Glan-Taylor prism in the vertical and horizontal directions, as indicated by the white arrow.

at the output of the 1.9-mm waveguide. The measured profiles are shown in Fig. 4(i,j). The vertically polarized wave is very similar to the Poynting vector distribution, as expected from a quasi-TM mode. After the prism though, a clearer zero line can be seen along the symmetry plane. The horizontal polarization pattern on the other hand is very different. While not perfectly symmetric as would be expected, it is clear that the intensity profile does not display a mirror symmetry in the horizontal direction. Note that both plots are normalized, the energy in the x' component is around 10% of the total output power.

In Fig. 4, our results are compared with the theoretical phase matching function:

$$|b(L)|^2 = |\kappa|^2 |a(0)|^4 \times \frac{e^{-\alpha_b L} + e^{-2\alpha_a L} - 2e^{-(\alpha_b/2 + \alpha_a)L} \cos(\Delta\beta L)}{(\alpha_a - \alpha_b/2)^2 + \Delta\beta^2}, \quad (10)$$

obtained by integrating equations (5) and (6) while neglecting the down-conversion term. To extract the experimental efficiency we use the theoretical maximum SH power: $|b(L)|^2 = |\kappa|^2 |a(0)|^4 L_{\text{eff}}^2$, where we introduced the effective interaction length $L_{\text{eff}} = 2(\exp(-\alpha_b L/2) - \exp(-\alpha_a L))/(2\alpha_a - \alpha_b)$. The input coupling and propagation loss of the pump are estimated to be 12 dB and 2.2 dB/mm respectively. The 775 nm propagation loss (9 dB/mm) was measured for a fundamental TE_{00} at 775 nm. We expect the propagation loss of the TM_{11} mode to be larger and hence report lower bounds of the experimental effective nonlinearity. Considering that we collect all the SH power through the high NA objective, we find $|\kappa_{\text{exp}}| > 27 (\sqrt{W_m})^{-1}$ for the short waveguide and $|\kappa_{\text{exp}}| > 68 (\sqrt{W_m})^{-1}$ for the long waveguide, in good agreement with the theory. Note that despite the large propagation loss, the spectral dependence of the process still resembles the standard sinc squared function. The experimental bandwidth matches very well with the theoretical one in both waveguides. Our results confirm the excitation of a TM_{11} SH mode by a TM_{00} pump mode in a III-V wire waveguide. This process is supported by the mixing of all six polarization components, highlighting the importance of full vectorial modeling when designing SHG experiments in III-V nanowires.

In conclusion, we designed two experiments to investigate the impact of longitudinal fields on second harmonic generation in III-V nanowires. We have demonstrated, through characterization of the propagation direction, spatial profiles, polarization and efficiency, the excitation of anti-symmetric modes through type I second harmonic generation. We theoretically showed that such coupling is enabled by the longitudinal components of the modes.

Integrated platforms are likely to play a large role in future optical systems. A good understanding of the physics of confined modes is hence crucial in developing all-optical computing. Our results show that, while they do not contribute to the time-averaged Poynting vector, longitudinal components store energy that can be harnessed for nonlinear conversion. With further dispersion engineering, this scheme can lead to ultra-efficient second harmonic generation [22], a process that finds applications in many fields including quantum circuits [26].

ACKNOWLEDGEMENTS

This work was supported by funding from the European Research Council (ERC) under the European Unions Horizon 2020 research and innovation programme (grant agreement Nos 726420, 759483 & 757800) and by the Fonds de la Recherche Fondamentale Collective (grant agreement No PDR.T.0185.18).

-
- * Electronic address: francois.leo@ulb.ac.be
- [1] C. Wang, C. Langrock, A. Marandi, M. Jankowski, M. Zhang, B. Desiatov, M. M. Fejer, and M. Lonar, *Optica* **5**, 1438 (2018).
 - [2] L. Chang, A. Boes, X. Guo, D. T. Spencer, M. J. Kennedy, J. D. Peters, N. Volet, J. Chiles, A. Kowligy, N. Nader, D. D. Hickstein, E. J. Stanton, S. A. Diddams, S. B. Papp, and J. E. Bowers, *Laser & Photonics Reviews* **12**, 1800149 (2018).
 - [3] M. Pu, L. Ottaviano, E. Semenova, and K. Yvind, *Optica* **3**, 823 (2016).
 - [4] B. Stern, X. Ji, Y. Okawachi, A. L. Gaeta, and M. Lipson, *Nature* **562**, 401 (2018).
 - [5] A. W. Snyder and J. D. Love, *Optical Waveguide Theory* (Chapman and Hall, London, 1983).
 - [6] J. B. Driscoll, X. Liu, S. Yasseri, I. Hsieh, J. I. Dadap, and R. M. Osgood, *Opt. Express* **17**, 2797 (2009).
 - [7] E. J. Bochove, G. T. Moore, and M. O. Scully, *Phys. Rev. A* **46**, 6640 (1992).
 - [8] A. S. van de Nes, J. J. M. Braat, and S. F. Pereira, *Rep. Prog. Phys.* **69**, 2323 (2006).
 - [9] L. Novotny, M. R. Beversluis, K. S. Youngworth, and T. G. Brown, *Phys. Rev. Lett.* **86**, 5251 (2001).
 - [10] R. W. Boyd, *Nonlinear Optics* (Academic, New York, 2003)
 - [11] S. A. Vahid and T. M. Monro, *Opt. Express* **17**, 2298 (2009).
 - [12] D. Dai and J. E. Bowers, *Opt. Express* **19**, 10940 (2011).
 - [13] Y. Kozawa and S. Sato, *J. Opt. Soc. Am. B*, **25**, 175 (2008).
 - [14] M. A. Baghban and K. Gallo, *APL Photonics* **1**, 061302 (2016).
 - [15] E. De Luca, R. Sanatinia, M. Mensi, S. Anand, and M. Swillo, *Phys. Rev. B* **96**, 075303 (2017).
 - [16] Y. Ueno, V. Ricci, and G. I. Stegeman, *J. Opt. Soc. Am. B* **14**, 1428 (1997).
 - [17] L. Alloatti, D. Korn, C. Weimann, C. Koos, W. Freude, and J. Leuthold, *Opt. Express* **20**, 20506 (2012).
 - [18] M. Kolesik and J. V. Moloney, *Phys. Rev. E* **70**, 036604 (2004).
 - [19] X. Chen, N. C. Panoiu, and R. M. Osgood, *IEEE Journal of Quantum Electronics* **42**, 160 (2006).
 - [20] B. A. Daniel and G. P. Agrawal, *J. Opt. Soc. Am. B* **27**, 956 (2010).
 - [21] K. Alexander, N. A. Savostianova, S. A. Mikhailov, B. Kuyken, and D. Van Thourhout, *ACS Photonics* **4**, 3039 (2017).
 - [22] C. Ciret, K. Alexander, N. Pouvellarie, M. Billet, C. Mas Arabi, B. Kuyken, S-P Gorza and F.Leo, to be submitted.
 - [23] U. D. Dave, B. Kuyken, F. Leo, S.-P. Gorza, S. Combrié, A. De Rossi, F. Raineri, and G. Roelkens, *Opt. Express* **23**, 4650 (2015).
 - [24] D. Duchesne, K. A. Rutkowska, M. Volatier, F. L egar e, S. Delprat, M. Chaker, D. Modotto, A. Locatelli, C. De Angelis, M. Sorel, D. N. Christodoulides, G. Salamo, R. Ars, V. Aimez, and R. Morandotti, *Opt. Express* **19**, 12408 (2011).
 - [25] R. Luo, Y. He, H. Liang, M. Li, and Q. Lin, *Optica* **5**, 1006 (2018).
 - [26] S. Zaske, A. Lenhard, C. A. Kessler, J. Kettler, C. Hepp,

C. Arend, R. Albrecht, W.-M. Schulz, M. Jetter, P. Michler, and C. Becher, Phys. Rev. Lett. **109**, 147404 (2012).